Multipath-Enhanced Device-Free Localization in Wideband Wireless Networks

Martin Schmidhammer, *Member, IEEE*, Christian Gentner, Stephan Sand, *Senior Member, IEEE*, and Uwe-Carsten Fiebig, *Senior Member, IEEE*

***Abstract*—State-of-the-art device free localization systems infer presence and location of users based on received signal strength measurements of line-of-sight links in wireless networks. In this letter, we propose to enhance device free localization systems by exploiting multipath propagation between the individual network nodes. Particularly, indoors, wireless propagation channels are characterized by multipath propagation, i.e., received signals comprise multipath components due to reflection and scattering. Given prior information about the surrounding environment, e.g., a floor plan, the individual propagation paths of multipath components can be derived geometrically. Inherently, these propagation paths differ spatially from the line-of-sight propagation path and can be considered as additional links in the wireless network. This extended network determines the novel multipath-enhanced device free localization system. Using theoretical performance bounds on the localization error, we show that including multipath components into device-free localization systems improves the overall localization performance and extends the coverage area significantly.**

***Index Terms*—Cramér–Rao lower bounds (CRLBs), device-free localization (DFL), multipath propagation, wireless sensor networks.**

I. Introduction

UBIQUITOUS connectivity and location-based services are key components for smart environments, such as modern manufacturing facilities and smart homes [1]. The demand in location awareness can be served, e.g., by active radio frequency (RF) based localization systems requiring the user to carry a localization device. Alternatively, passive localization systems estimate presence and location of the user by measuring the user's impact on the propagation of RF signals. We distinguish thereby between radar systems exploiting properties of directly reflected and scattered signals, as in [2], and device-free localization (DFL) systems exploiting user-induced power changes of received signals within wireless networks due to diffraction and shadowing, as in [3]. Unlike classic radar, DFL can be deployed using arbitrary underlying wireless networks, ranging from ZigBee [3] to ultrawideband (UWB) [4]. Typically, DFL systems measure the received signal strength (RSS) between network nodes. Based on these RSS measurements, the location is either estimated by computing propagation field images, so-called radio tomographic imaging [3], or by using empirical [5] or theoretical propagation models [6], [7], which directly relate the RSS measurements to the user location.

Manuscript received December 16, 2020; revised January 13, 2021; accepted January 14, 2021. Date of publication January 18, 2021; date of current version April 7, 2021. *(Corresponding author: Martin Schmidhammer.)*

The authors are with the Institute of Communications and Navigation, German Aerospace Center, 82234 Wessling, Germany (e-mail: martin.schmidhammer@dlr.de; christian.gentner@dlr.de; stephan.sand@dlr.de; uwe.fiebig@dlr.de).

Digital Object Identifier 10.1109/LAWP.2021.3052438

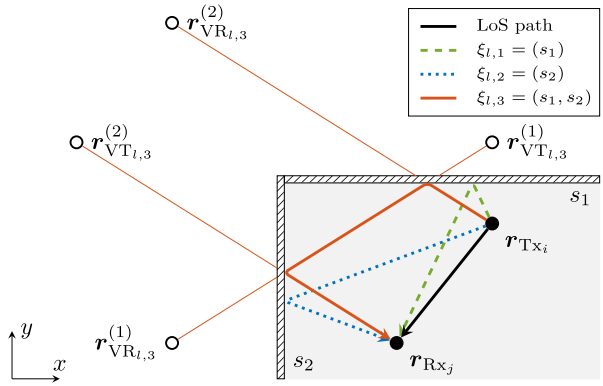

Fig. 1. Exemplary multipath propagation for network link l (Tx_i and Rx_j) in a given environment with two reflecting surfaces $\mathcal{S} = \{s_1, s_2\}$. Arrows indicate the physical propagation paths of LoS and MPCs according to the set of visible sequences $\mathcal{X}_l = \{\xi_{l,1}, \xi_{l,2}, \xi_{l,3}\}$. The geometric decomposition is illustrated for the second-order reflection $\xi_{l,3}$ by VTs and VRs at mirrored positions of Tx_i and Rx_j. Resulting equidistant paths between pairs of corresponding nodes are indicated by red lines reconstructing the physical propagation path of the MPC within the observation area.

Prevalent DFL systems deploy narrowband RF devices, and thus, besides the user impact, the RSS is also affected by small-scale multipath fading. Since multipath fading is unique for each network link, narrowband DFL systems require extensive initial calibration and frequent recalibration accounting for time-variant propagation environments [8]. Addressing the issues of multipath fading, Beck *et al.* [9] propose to use UWB devices for DFL systems. Thereby, the wide signal bandwidth enables the separation of the received signal into line-of-sight (LoS) and multipath components (MPCs). The extraction of MPCs allows to isolate the LoS signal and, thus, to mitigate distortions due to multipath propagation.

Instead of mitigating distortions of the LoS signal, we propose to make particular use of multipath propagation for improving DFL systems. The proposed novel multipath-enhanced device-free localization (MDFL) systems are strongly motivated by the measurements in [10]. These measurements demonstrate that user-induced fading can be also observed in the received power of reflected and scattered signals. Naturally, the propagation paths of these reflected and scattered signals differ spatially from the LoS propagation path (see Fig. 1), and thus, contain spatial information in addition to that of the LoS paths. The goal of this letter is to illustrate the performance improvement of DFL systems that can be obtained by incorporating propagation paths

of reflected and scattered signals as additional links to the underlying wireless network. We provide the signal processing to extract the spatial information from each pair of transmitting and receiving node and derive the theoretical performance bounds on the localization error for the novel MDFL system. In a case study, we evaluate MDFL numerically and quantify the improvement compared to common DFL.

II. Network and Propagation Model

We consider an MDFL system relying on a network of N_{Tx} transmitting and N_{Rx} receiving nodes at known locations $\boldsymbol{r}_{\mathrm{Tx}_i}$, $i \in \{1, \ldots, N_{\mathrm{Tx}}\}$, and $\boldsymbol{r}_{\mathrm{Rx}_j}$, $j \in \{1, \ldots, N_{\mathrm{Rx}}\}$. Receiving nodes can be collocated with transmitting nodes or individually placed. The network link configuration is determined by the index set $\mathcal{P}$, where link $(i, j) \in \mathcal{P}$ is composed of the ith transmitting and the jth receiving node and is indexed by $l \in \{1, \ldots, |\mathcal{P}|\}$. For link l, the signal at the receiving node is modeled as a superposition of scaled and delayed replica of a known transmit signal $s_l(t)$ of duration T_{sym}. These comprise the LoS and a finite number of static MPCs due to reflections of the surrounding environment. Therewith, the received signal is expressed as

$$y_l(t) = \sum_{m=1}^{N_l} \alpha_{l,m}(t) s_l(t - \tau_{l,m}) + n_l(t) \tag{1}$$

with time-variant, complex amplitude $\alpha_{l,m}(t)$, and static propagation delay $\tau_{l,m}$ of the mth MPC [11]. For notational convenience, we omit the time index for the amplitude and consider LoS paths also as MPCs. The term $n_l(t)$ denotes white circular symmetric normal distributed noise with variance $\sigma^2_{y_l}$.

Following Meissner *et al.* [12] and Gentner *et al.* [13], we model the delays of the MPCs geometrically using virtual nodes. Therefore, we represent the surrounding environment by a finite number of reflecting surfaces determining the set $\mathcal{S}$. For this representation, we require prior information about the surrounding environment, which can be provided, e.g., by a floor plan [12]. Based on the set of reflecting surfaces $\mathcal{S}$, we can define reflection sequences that chronologically describe the signal propagation for an MPC p from the transmitting to the receiving node of link l. Using tuple notation, we express these sequences as $\xi_{l,p} = (s_b)$ with $s_b \in \mathcal{S}$, where the sequence length, denoted as $N_{\xi_{l,p}}$, is determined by the order of reflection. Subsequently, we can compose a set $\mathcal{X}$ containing all potential reflection sequences. Based on these sequences, we can construct virtual transmitters (VTs) and virtual receivers (VRs) for each MPC of the network links by consecutively mirroring the physical nodes. Note that due to symmetry, VRs are constructed using the sequences in reverse order. For sequence $\xi_{l,p} \in \mathcal{X}$, the locations of the virtual nodes are thus denoted by $\boldsymbol{r}^{(u)}_{\mathrm{VT}_{l,p}}$ and $\boldsymbol{r}^{(N_{\xi_{l,p}}-u)}_{\mathrm{VR}_{l,p}}$, where the index $u \in \{0, \ldots, N_{\xi_{l,p}}\}$ corresponds to pairs of related virtual nodes. Thereby, the physical transmitting and receiving nodes are referred to as $\boldsymbol{r}^{(0)}_{\mathrm{VT}_{l,p}}$ and $\boldsymbol{r}^{(0)}_{\mathrm{VR}_{l,p}}$, respectively. Fig. 1 provides an example for a second-order reflection illustrating the sets of VTs and VRs. It is noticeable that the distances between the pairs of related nodes are equal. Due to geometry, these distances correspond to the length of the physical propagation path. Thus, we can express this length for any pair of related nodes u as

$$d\left(\xi_{l,p}\right) = d_{l,p} = \|\boldsymbol{r}^{(u)}_{\mathrm{VT}_{l,p}} - \boldsymbol{r}^{(N_{\xi_{l,p}}-u)}_{\mathrm{VR}_{l,p}}\|. \tag{2}$$

Furthermore, as shown in Fig. 1, the paths between pairs of related nodes intersect at the physical reflection points. Thus, we can reconstruct the physical propagation paths geometrically similar to optical ray-tracing [12]. This allows to compose a set of visible sequences $\mathcal{X}_l \subseteq \mathcal{X}$ for each network link, with cardinality $|\mathcal{X}_l| = N_l$ equal to the number of MPCs modeled in (1). Finally, we can define a set of possible path lengths as

$$\mathcal{D}_l = \{d(\xi_{l,m}) \,|\, \xi_{l,m} \in \mathcal{X}_l\}. \tag{3}$$

III. Multipath-Enhanced DFL

The objective of any DFL system is to estimate the user state, defined as location and velocity, based on user-induced changes in the received signal power. Following a Bayesian approach, this objective can be expressed by a transition model describing the spatiotemporal evolution of the user state, and a measurement model relating the measured changes in the received signal power to the user state. In the following, we describe the required signal processing and provide a corresponding measurement model.

A. Initialization and Data Association

Initially, we need to determine the individual propagation effects of the static environment. In the initialization step, the channel of each network link is therefore observed over a period T_{ini}. Ideally, the environment should be devoid of any user during this period. This ensures that we can accurately describe the propagation effects of the static environment. With T_{g} as time interval between two adjacent received signals, a total of $\lfloor T_{\mathrm{ini}}/T_{\mathrm{g}} \rfloor$ consecutive signal samples are collected. For each signal sample, we determine amplitude and delay values for $\hat{N}_l$ separable MPCs using maximum likelihood estimation, e.g., using the space-alternating generalized expectation-maximization algorithm [14].

By averaging the amplitude and delay estimates over the amount of signal samples, we obtain the set of mean amplitude $\{\bar{\alpha}_{l,q}\}_{q=1}^{\hat{N}_l}$ and the set of mean delay $\{\bar{\tau}_{l,q}\}_{q=1}^{\hat{N}_l}$. The set of mean amplitude allows to calculate the power of the MPCs for the idle channel, which serves as reference to determine user-induced power changes. The set of mean delay determines the set of estimated path lengths as

$$\hat{\mathcal{D}}_l = \{c \cdot \bar{\tau}_{l,q} \,|\, 1 \leq q \leq \hat{N}_l\}. \tag{4}$$

After the initialization step, i.e., the estimation of all observable MPCs from the received signals, we need to determine the physical propagation paths of these MPCs. In Section II, we have modeled the delays of MPCs using virtual nodes and reflection sequences in a preinitialization step. Thereby, a reflection sequence describes chronologically the signal propagation from transmitting to receiving node and represents the physical propagation path, accordingly. Thus, we can relate the MPCs estimated during initialization to the physical propagation paths modeled in the preinitialization step.

The MPCs are characterized by delay or path length, respectively. We therefore use the corresponding sets of expected and estimated path lengths for data association, i.e., $\mathcal{D}_l$ in (3) and $\hat{\mathcal{D}}_l$ in (4). A possible association approach provide Meissner *et al.* [12], following optimal subpattern assignment [15]. Thereby, the sets $\mathcal{D}_l$ and $\hat{\mathcal{D}}_l$ are matched such that the cumulative

distance between expected and estimated path lengths is minimized. The individual associations are further constrained not to exceed a certain distance value, the so-called cutoff value. The cutoff value is defined by the ranging accuracy of the transmitted signals [12]. Therewith, we discard strongly outlying MPCs and avoid wrong associations. Clutter due to diffuse reflections and scattering is thus inherently eliminated.

The constrained data association is applied for each network link l resulting in sets of associated reflection sequences $\check{\mathcal{X}}_l$. Depending on the observed MPCs during the initialization and the subsequent association step, the set $\check{\mathcal{X}}_l$ of network link l contains an individual number of $\check{N}_l$ associated sequences. Combining the information from all network links results in the union set $\check{\mathcal{X}} = \cup_{l=1}^{|\mathcal{P}|} \check{\mathcal{X}}_l$. Eventually, the cardinality $|\check{\mathcal{X}}| = \sum_{l=1}^{|\mathcal{P}|} \check{N}_l$ determines the overall amount of associated reflection sequences and, thus, the amount of corresponding MPCs, which can be used for MDFL. Note that the association step is crucial since MDFL relies on the location information contained in the propagation paths. Misassociated MPCs could therefore even degrade the localization performance.

B. Parameter Estimation and Measurement Model

After initialization and data association, the network is basically ready for localization, but requires measurement data. Therefore, we continuously determine the amplitude values of all associated MPCs of each network link. For each $\xi_{l,n} \in \check{\mathcal{X}}$ with corresponding delay $\bar{\tau}_{l,n}$, we estimate the amplitude using

$$\hat{\alpha}_{l,n} = \hat{\alpha}(\bar{\tau}_{l,n}) = \int_0^{T_{\text{sym}}} \left(y_{l,n}^{\text{res}}(t)\right)^* s_l(t - \bar{\tau}_{l,n})\, dt \tag{5}$$

as the projection of the residuum signal $y_{l,n}^{\text{res}}(t)$ onto the unit transmit signal $s_l(t)$ [12]. Thereby, the residuum signal is defined as received signal adjusted for all MPCs up to the $(n-1)$th, i.e., $y_{l,n}^{\text{res}}(t) = y_l(t) - \sum_{n'=1}^{n-1} \hat{\alpha}_{l,n'} s_l(t - \bar{\tau}_{l,n'})$.

Given the amplitude estimates, we can calculate the measured power of an MPC as $|\hat{\alpha}_{l,n}|^2$ and express the user-induced power changes by adjusting the measured power by the power of the idle channel determined during initialization. Thus, we can compose the measurement vector $\mathbf{z} \in \mathbb{R}^{|\check{\mathcal{X}}|}$, defined in decibel, by stacking the individual components $\mathrm{z}_{l,n} = 20 \log_{10} \frac{|\hat{\alpha}_{l,n}|}{|\bar{\alpha}_{l,n}|}$.

The estimation steps described earlier were successfully applied to measurement data in [10]. The results were used to validate a physical model for user-induced fading on the power of MPCs. In this letter, we adopt the model derived in [10] and slightly modify it for simplification. We therefore carefully approximate the user impact on individual pairs of related nodes by the empirical exponential model as in [5]. Thus, we can model the power changes of an MPC depending on the user location $\boldsymbol{r}$ as the sum

$$f(\boldsymbol{r}, \xi_{l,n}) = \sum_{u=0}^{N_{\xi_{l,n}}} \phi_{l,n} e^{-\delta_{l,n}^{(u)}(\boldsymbol{r})/\kappa_{l,n}} \tag{6}$$

where $\phi_{l,n}$ defines the maximum modeled power change in decibel and $\kappa_{l,n}$ expresses the spatial decay rate. The excess path length $\delta_{l,n}^{(u)}(\boldsymbol{r})$ of the uth pair of virtual nodes, as defined by sequence $\xi_{l,n}$, is calculated by

$$\delta_{l,n}^{(u)}(\boldsymbol{r}) = \|\boldsymbol{r}_{\mathrm{VT}_{l,n}}^{(u)} - \boldsymbol{r}\| + \|\boldsymbol{r}_{\mathrm{VR}_{l,n}}^{(N_{\xi_{l,n}}-u)} - \boldsymbol{r}\| - d_{l,n} \tag{7}$$

with the path length $d_{l,n}$ being defined in (2). Eventually, we can model the measurement vector defined in decibel as

$$\mathbf{z} = [\ldots, f(\boldsymbol{r}, \xi_{l,n}), \ldots]^{\mathrm{T}} + \mathbf{w} \quad \forall l, n : \xi_{l,n} \in \check{\mathcal{X}} \tag{8}$$

with Gaussian measurement noise $\mathbf{w} \sim \mathcal{N}(\mathbf{0}, \mathbf{R}(\boldsymbol{r}))$. Assuming mutually independent measurements, the noise covariance matrix $\mathbf{R}(\boldsymbol{r}) \in \mathbb{R}^{|\check{\mathcal{X}}| \times |\check{\mathcal{X}}|}$ is diagonal. For clarity of presentation and avoiding complexity, in this letter, the elements of the noise covariance matrix are assumed to be independent of user location $\boldsymbol{r}$, i.e., $\sigma_{l,n}^2(\boldsymbol{r}) = \sigma_{l,n}^2$ and therewith $\mathbf{R}(\boldsymbol{r}) = \mathbf{R}$.

IV. Performance Bound

The Cramér–Rao lower bound (CRLB) provides a lower bound on the variance of an unbiased estimator, defined by the inverse of the Fisher information matrix (FIM). Therefore, the unbiased estimator $\hat{\boldsymbol{r}}$ of user location $\boldsymbol{r} = [r_x, r_y, r_z]^{\mathrm{T}}$ satisfies $\mathrm{Cov}(\hat{\boldsymbol{r}}) = \mathrm{E}[(\hat{\boldsymbol{r}} - \boldsymbol{r})(\hat{\boldsymbol{r}} - \boldsymbol{r})^{\mathrm{T}}] \leq \mathbf{F}(\boldsymbol{r})^{-1}$, where $\mathbf{F}(\boldsymbol{r}) \in \mathbb{R}^{3\times 3}$ denotes the FIM. Given the Gaussian measurement model (8) with noise covariance matrix $\mathbf{R}$, which, for simplicity, is assumed to be independent of the user location, we can express the FIM as

$$\mathbf{F}(\boldsymbol{r}) = \mathbf{J}(\boldsymbol{r})^{\mathrm{T}} \mathbf{R}^{-1} \mathbf{J}(\boldsymbol{r}) \tag{9}$$

where $\mathbf{J}(\boldsymbol{r}) \in \mathbb{R}^{|\check{\mathcal{X}}| \times 3}$ denotes the Jacobian matrix of the measurement model with respect to the user location [6]. Using the differential operator $\nabla_{\boldsymbol{r}} = [\frac{\partial}{\partial r_x}, \frac{\partial}{\partial r_y}, \frac{\partial}{\partial r_z}]^{\mathrm{T}}$, the elements of the Jacobian matrix, which correspond to $\xi_{l,n}$, are calculated as

$$\begin{aligned} [\mathbf{J}(\boldsymbol{r})]_{\xi_{l,n}} &= \nabla_{\boldsymbol{r}} f(\boldsymbol{r}, \xi_{l,n}) \\ &= \frac{\phi_{l,n}}{\kappa_{l,n}} \sum_{u=0}^{N_{\xi_{l,n}}} e^{-\delta_{l,n}^{u}(\boldsymbol{r})/\kappa_{l,n}} \nabla_{\boldsymbol{r}} \delta_{l,n}^{u}(\boldsymbol{r}) \end{aligned} \tag{10}$$

with

$$\nabla_{\boldsymbol{r}} \delta_{l,n}^{u}(\boldsymbol{r}) = \frac{\boldsymbol{r}_{\mathrm{VT}_{l,n}}^{(u)} - \boldsymbol{r}}{\|\boldsymbol{r}_{\mathrm{VT}_{l,n}}^{(u)} - \boldsymbol{r}\|} + \frac{\boldsymbol{r}_{\mathrm{VR}_{l,n}}^{(N_{\xi_{l,n}}-u)} - \boldsymbol{r}}{\|\boldsymbol{r}_{\mathrm{VR}_{l,n}}^{(N_{\xi_{l,n}}-u)} - \boldsymbol{r}\|}. \tag{11}$$

For the evaluation of the localization accuracy, we can use the CRLB to determine the root-mean-square error (RMSE) of the location estimate. Based on the diagonal elements of the CRLB, the RMSE is lower bounded by

$$\mathrm{RMSE} = \sqrt{\mathrm{E}\left[\|(\hat{\boldsymbol{r}} - \boldsymbol{r})\|^2\right]} \leq \sqrt{\mathrm{tr}\left(\mathbf{F}(\boldsymbol{r})^{-1}\right)}. \tag{12}$$

V. Numerical Results

Finally, we evaluate the performance of the proposed MDFL approach numerically for a fully meshed network of $N_{\mathrm{Tx}} = N_{\mathrm{Rx}} = 20$ circularly arranged, collocated transmitting, and receiving nodes. Each node has a distance of 4 m to the network center. All nodes are located at the same height and correspond to the height of the body center of the user. Thus, both the network nodes and the evaluated user locations are placed on the same plane. The multipath propagation environment is characterized by four reflecting surfaces confining an observation area of 23 m × 15.5 m. The exact arrangement of the setup is shown to scale in Fig. 2.

For the numerical analysis, we have refrained from an explicit simulation of the signal estimation process at the receiving

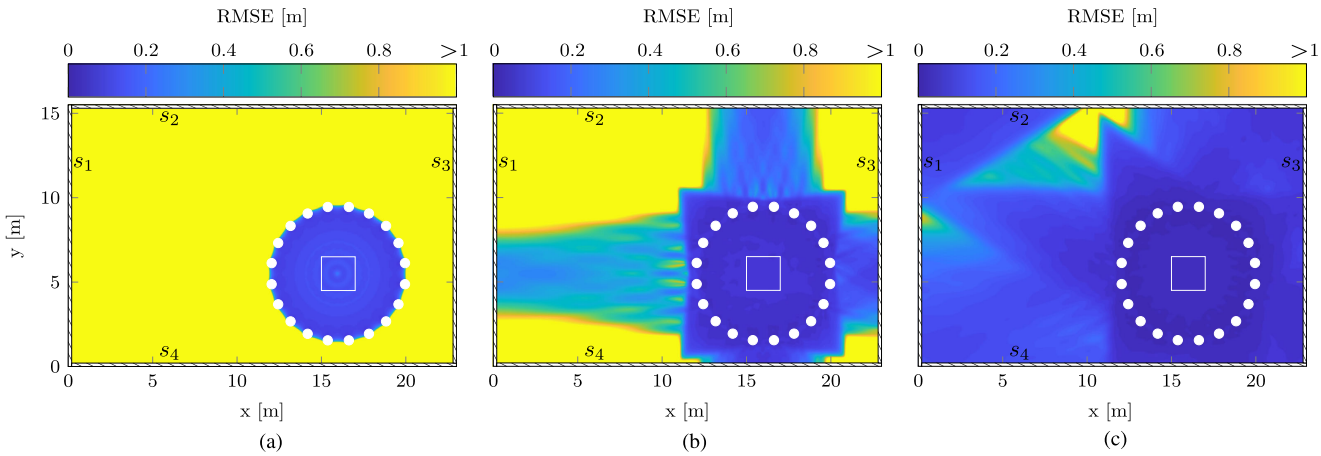

Fig. 2. CRLB limit to the localization accuracy of DFL and MDFL systems. The underlying network is identical for each system and consists of 20 circularly arranged transceiving nodes, as indicated by white bold dots. The observation area is confined by reflecting surfaces $\mathcal{S} = \{s_1, s_2, s_3, s_4\}$ represented by hatched lines. A DFL system with LoS signals only is considered in (a), MDFL systems with LoS and first-order reflections in (b), and with LoS, first- and second-order reflections in (c). The white rectangle in the network center defines an area of 2 m $\times$ 2 m used to calculate the expected RMSE (cf., Fig. 3).

nodes. Instead, we assume perfect association of all considered MPCs. This implies that all components of the received signals within the network are assumed to be perfectly estimated and then correctly associated with the respective reflecting sequences (cf., Section III-A). Reflections from ground and ceiling are not taken into account. However, it can be assumed that MPCs due to these reflections would further improve the performance of MDFL. The parameter set of the measurement model is assumed as $\phi_{l,n} = -2.5$ dB, $\kappa_{l,n} = 0.05$ m, and $\sigma_{l,n} = 1.5$ dB $\quad \forall l, n$ [8]. Using (12), the localization accuracy is evaluated in terms of RMSE. For assessing the spatial localization capabilities, we define the area in which a localization approach achieves an RMSE < 1 m as coverage area.

The localization accuracy is calculated for state-of-the-art DFL, as shown in Fig. 2, and for two MDFL systems complementing the network by all possible MPCs due to first- and second-order reflections, as shown in Fig. 2(b) and (c). It can be seen that the DFL and MDFL systems cover the area between the network nodes with high localization accuracy. For DFL, however, this area coincides with the coverage area. In contrast, the coverage areas of the considered MDFL systems span over the entire observation area. In particular, MDFL, including MPCs of second-order reflections, covers the observation area almost completely.

Apart from a larger coverage, the results in Fig. 2(a)–(c) indicate that also the absolute localization accuracy has improved for MDFL compared to DFL. To further investigate this performance improvement, we calculate an expected RMSE for an area of 2 m $\times$ 2 m located in the network center, as marked in Fig. 2. The expected RMSE is determined for different numbers of network nodes, different orders of reflections, and a varying environment. As before, fully meshed networks of circularly arranged transceiving nodes are assumed. The resulting values are shown in Fig. 3. For each environment, the expected RMSE monotonically decreases with the number of nodes. Overall, the localization accuracy improves with an increasing number of considered reflection surfaces and higher orders of reflection, which both increase the number of MPCs. Hence, rich multipath environments are beneficial for MDFL. The highest accuracy gain can be achieved for networks employing only a few nodes.

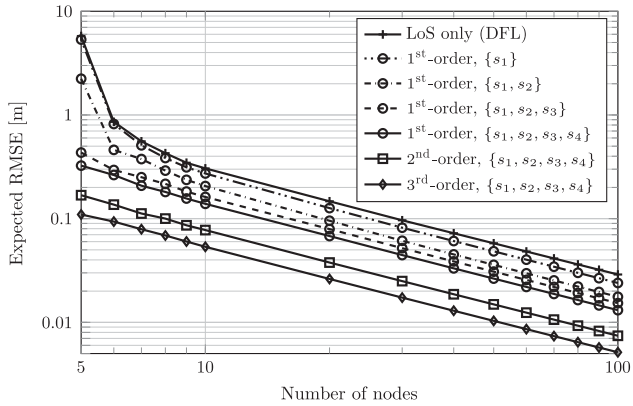

Fig. 3. Expected RMSE as a function of network nodes, calculated for an area of 2 m $\times$ 2 m in the network center (cf., Fig. 2). The evaluated MDFL systems consider in addition to LoS paths also propagation paths of first-, second-, and third-order reflections from surfaces $\mathcal{S} = \{s_1, s_2, s_3, s_4\}$.

Sparse networks benefit particularly from multipath propagation, since MPCs compensate for the lack of measurements from additional nodes.

VI. Conclusion

In this letter, we introduce a multipath-enhanced DFL approach. For this novel approach, we provide a geometrical model describing the physical propagation of MPCs and the corresponding signal processing. Based on the underlying measurement model, we derive the theoretical performance bound on the localization error allowing to evaluate the proposed approach numerically. The results show that the consideration of MPCs overcomes the constrained spatial localization capabilities of state-of-the-art DFL approaches and extends the coverage area significantly. Moreover, the localization accuracy improves with increasing number of MPCs, especially for sparse networks.

REFERENCES

[1] R. C. Shit *et al.*, "Ubiquitous localization (UbiLoc): A survey and taxonomy on device free localization for smart world," *IEEE Commun. Surveys Tuts.*, vol. 21, no. 4, pp. 3532–3564, Oct.–Dec. 2019.

[2] M. Govoni, F. Guidi, E. M. Vitucci, V. D. Esposti, G. Tartarini, and D. Dardari, "Ultra-wide bandwidth systems for the surveillance of railway crossing areas," *IEEE Commun. Mag.*, vol. 53, no. 10, pp. 117–123, Oct. 2015.

[3] J. Wilson and N. Patwari, "Radio tomographic imaging with wireless networks," *IEEE Trans. Mobile Comput.*, vol. 9, no. 5, pp. 621–632, May. 2010.

[4] N. Patwari and J. Wilson, "RF sensor networks for device-free localization: Measurements, models, and algorithms," *Proc. IEEE*, vol. 98, no. 11, pp. 1961–1973, Nov. 2010.

[5] Y. Guo, K. Huang, N. Jiang, X. Guo, Y. Li, and G. Wang, "An exponential-Rayleigh model for RSS-based device-free localization and tracking," *IEEE Trans. Mobile Comput.*, vol. 14, no. 3, pp. 484–494, Mar. 2015.

[6] V. Rampa, S. Savazzi, M. Nicoli, and M. D'Amico, "Physical modeling and performance bounds for device-free localization systems," *IEEE Signal Process. Lett.*, vol. 22, no. 11, pp. 1864–1868, Nov. 2015.

[7] V. Rampa, G. G. Gentili, S. Savazzi, and M. D'Amico, "EM models for passive body occupancy inference," *IEEE Antennas Wireless Propag. Lett.*, vol. 16, pp. 2517–2520, 2017.

[8] O. Kaltiokallio, R. Jäntti, and N. Patwari, "ARTI: An adaptive radio tomographic imaging system," *IEEE Trans. Veh. Technol.*, vol. 66, no. 8, pp. 7302–7316, Aug. 2017.

[9] B. Beck, X. Ma, and R. Baxley, "Ultrawideband tomographic imaging in uncalibrated networks," *IEEE Trans. Wireless Commun.*, vol. 15, no. 9, pp. 6474–6486, Sep. 2016.

[10] M. Schmidhammer, M. Walter, C. Gentner, and S. Sand, "Physical modeling for device-free localization exploiting multipath propagation of mobile radio signals," in *Proc. 14th Eur. Conf. Antennas Propag*., Apr. 2020, pp. 1–5.

[11] A. F. Molisch, "Ultra-wide-band propagation channels," *Proc. IEEE*, vol. 97, no. 2, pp. 353–371, Feb. 2009.

[12] P. Meissner, E. Leitinger, and K. Witrisal, "UWB for robust indoor tracking: Weighting of multipath components for efficient estimation," *IEEE Wireless Commun. Lett.*, vol. 3, no. 5, pp. 501–504, Oct. 2014.

[13] C. Gentner, T. Jost, W. Wang, S. Zhang, A. Dammann, and U. Fiebig, "Multipath assisted positioning with simultaneous localization and mapping," *IEEE Trans. Wireless Commun.*, vol. 15, no. 9, pp. 6104–6117, Sep. 2016.

[14] B. H. Fleury, M. Tschudin, R. Heddergott, D. Dahlhaus, and K. I. Pedersen, "Channel parameter estimation in mobile radio environments using the SAGE algorithm," *IEEE J. Sel. Areas Commun.*, vol. 17, no. 3, pp. 434–450, Mar. 1999.

[15] D. Schuhmacher, B.-T. Vo, and B.-N. Vo, "A consistent metric for performance evaluation of multi-object filters," *IEEE Trans. Signal Process.*, vol. 56, no. 8, pp. 3447–3457, Aug. 2008.